03

A spiral long-periodic structure of the turbulent flow core in a heated rectangular duct with inclined ribs at a wall

© S.A. Galaev, A.M. Levchenya, V.V. Ris, E.M. Smirnov

Peter the Great Saint-Petersburg Polytechnic University,
195251 St. Petersburg, Russia
e-mail: sealga@mail.ru

Received July 5, 2024
Revised August 20, 2024
Accepted September 15, 2024

Paper presents the results of the numerical modeling of the turbulent airflow in a rectangular duct 50 caliber length, on one wall of which straight ribs inclined to the axis of the channel at an angle of 45° are periodically located. The simulation covered the range of the Reynolds number from 10^4 to $2 \cdot 10^5$. It has been established that with all Re number values the long areas of statistically stationary spiral flow are formed. Specific phases of the spiral flow structures formation have been identified as they developed from the channel entrance. It is shown that the parameters (friction and heat transfer) of the flow with developed spiral structures are close to the parameters of the spatially periodic flow with the same Re number. The presence of specific phases of the spiral flow formation obtained in a numerical modeling are confirmed with the presented in the literature results of physical experiments.

Keywords: ribbed duct, turbulent flow, entry region, spiral flow, heat transfer.

DOI: 10.61011/TP.2024.11.59744.221-24

Introduction

Turbulent flows and heat transfer in rectangular channels with internally ribbed walls have been studied by methods of physical and numerical modeling for a long time (see, for example, monographs [1,2]). The interest in research is associated with the use of such channels for cooling blades of high-temperature gas turbines [3] and for heating various media in the channels of heat exchange devices, in particular, devices that absorb solar radiation [4].

Rational geometric parameters have been established for different ribbing options to date. One of the variants is characterized by the following parameters: straight ribs with square section $e \times e$ ($e = 0.1H$) are arranged in parallel in a straight rectangular channel with $W/H = 1.5$ (W and H — width and height of the section) across one of the walls with a width of W and pitch of P, equal to H, these ribs are inclined relative to the longitudinal axis of the channel by an angle α, which ranges from 45° to 60° for a significant increase of heat transfer [3].

The experimental studies for the case of $\alpha = 45°$ (Fig. 1), for $W/H = 1.5$, $P = H$ and $e = 0.1H$ were conducted in particular by the author of the paper [5]. The flow of air in a channel including a section with twelve ribs, as well as inlet and outlet plain sections, was studied in this experiment. It was found that the intensification of heat transfer on plain sections of the ribbed wall, compared with heat transfer in a plain channel, is 60−70%, and the level of intensification decreases with an increase of the Re number from 10^5 to $1.8 \cdot 10^5$; here $\mathrm{Re} = U_b D_h/\nu$, where U_b — average bulk velocity, D_h — hydraulic diameter, ν — kinematic viscosity.

The authors of this paper, for conditions close to those accepted in the experiments [5], performed numerical modeling of the developed turbulent flow and heat transfer in a channel with a ribbed wall, assuming the periodicity of the flow field with a rib pitch P [6]. Calculations based on the Reynolds equations using SST $k-\omega$ turbulence models showed [6] that the degree of heat transfer intensification

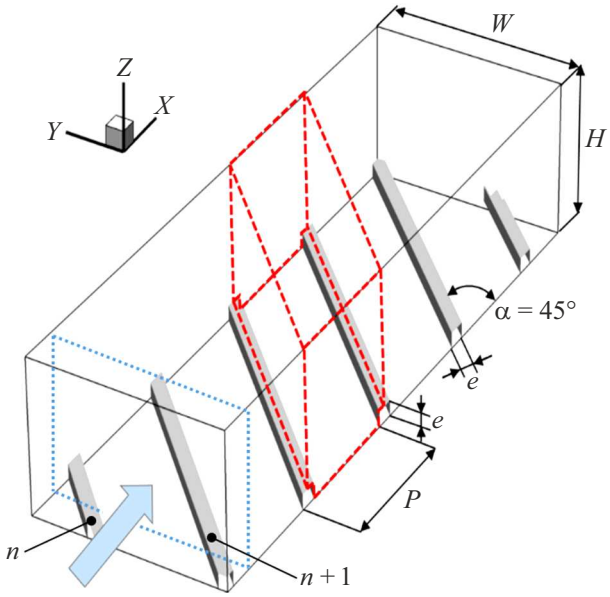

Figure 1. Section of the channel with one ribbed wall. Red dashed lines — channel segment boundaries, blue dotted lines — channel section boundaries normal to the longitudinal axis x, arrow — flow direction, n and $n+1$ — the numbering order of the ribs in the channel.

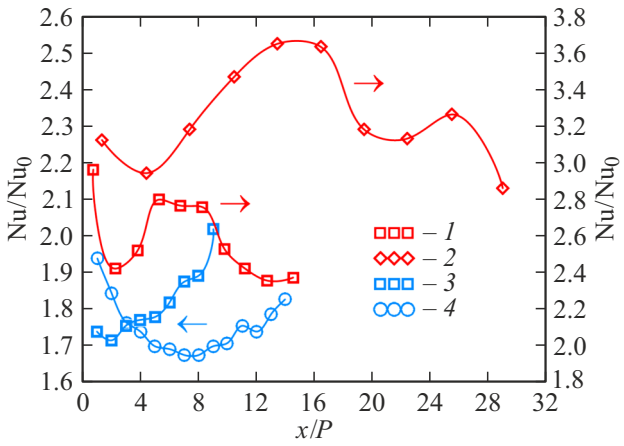

Figure 2. Results of experiments for the intensification of heat transfer in ribbed channels: *1, 2* — data [7], *3, 4* — data [8].

in the range of the Re number from $5 \cdot 10^4$ to $2 \cdot 10^5$ is 77–79%, slightly increasing with the increase of Re. A very moderate discrepancy between the results of physical and numerical experiments was attributed primarily to the difference in the real flow in the channel, which includes only twelve ribbed segments [5], from a kind of idealized flow with longitudinal periodicity, investigated in [6] by numerical modeling. At the same time, we would like to note that when choosing the working area, the author of the experimental study [5] relied on a very common opinion about the stabilization of the flow and the establishment of heat transfer characteristics during the first four ribbed sections [3].

Let us turn to other experimental studies of heat transfer during turbulent air flow in rectangular channels with one-sided ribbing [7,8]. The ribs had a square cross section in both studies and were installed at an angle of 45° relative to the longitudinal axis of the channel. The heat transfer in a square-section channel ($H \times H$) with two opposite ribbed walls was studied in Ref. [7]. The channel included up to 33 ribbed sections and had no pre-connected plain section. The heat transfer in a channel with a cross section $W/H = 5$ and one or two ribbed wide walls was studied in Ref. [8]; the number of ribs installed with pitch H on a wall of greater width was sixteen, an extended section of a plain channel was provided before the entrance of the ribbed section of the channel.

Some of the results of these studies are shown in summary Fig. 2. The values of the ratio of the longitudinal coordinate x to the pitch between the ribs P are plotted on the abscissa axis. The values of the ratio of the Nusselt number in the ribbed channel (Nu) to the Nusselt number of a developed flow and stabilized heat exchange in a plain channel of the same cross section (Nu_0) are plotted on the ordinate axis. The values of the Nu number are obtained by averaging the local parameters over the area of each interrib space. The curves 1 – 4 correspond to the following geometric and mode parameters: red lines and symbols *1* and *2* — $W/H = 1$, $\mathrm{Re} = 3 \cdot 10^4$, $e/H = 0.1$, moreover, *1* – $P/H = 1$, *2* — $P/H = 0.5$ [7]; blue lines and symbols *3* and *4* — $W/H = 5$, $\mathrm{Re} = 2.9 \cdot 10^4$, $e/H = 0.15$, moreover, *3* –$P/H = 1.5$, *4* — $P/H = 1$ [8].

The above experimental data and a number of other data presented in the literature indicate the non-monotonic nature of the change in heat transfer along the ribbed channels. Fig. 2 shows variants *1, 2* and *4* in which a heat transfer reduction area is observed immediately after the entrance, which in only one case (variant *4*) extends approximately to the eighth rib, and in other cases it is limited to the length of two-four pitches. Further, the heat transfer either increases almost monotonously, like in variants *3* and *4* (channel with $W/H = 5$), or its behavior becomes undulating, like in variants *1* and *2* (channel with $W/H = 1$). For the variant *1*, the amplitude of the $\mathrm{Nu}/\mathrm{Nu}_0$ „wave“ is close to 10% of the average value, and the amplitude reaches 18% for the variant *2*. It is appropriate to note here that the values of the Nusselt number decrease monotonously in plain channels, following a hyperbolic dependence of the type $a_1 - a_2/(x/D_h)^b$, in which a_1, a_2 and b — values depending on geometry channels, Re and Pr numbers. For example, a dependence is proposed in [9], in which $a_1 = 1$, $a_2 \propto \mathrm{Re}^{-0.23}$ and $b \approx 0.8$ is a value that weakly depends on the Re number.

The number of ribbed segments, as a rule, does not exceed two dozen in experimental studies and in rare cases reaches three dozen. The mentioned features of the experimental data obtained for relatively short channels and the observed discrepancies with the results of solving the idealized problem posed under the assumption of longitudinal periodicity ensure the relevance of the task of numerical modeling of turbulent flow and heat transfer developing in a significantly elongated channel, the number of segments in which far exceeds the values assumed in known experimental studies.

The formulation of the problem of numerical simulation of flow and heat transfer in a long channel with a single ribbed wall presented below was largely based on the author's experience in numerical analysis of hydrodynamic and heat exchange processes presented in Ref. [6], obtained under the assumption of their longitudinal periodicity with a rib spacing. It is most important here to note the experience of numerical reproduction and analysis of a system of statistically stationary vortices, which are formed by inclined ribs and are the reason for an increase in heat transfer and hydraulic resistance in a channel with a ribbed wall.

A general idea of the vortex structure of a turbulent periodic flow formed in a channel with a rib installation angle of $\alpha = 45°$ is given in Fig. 3. Inclined ribs, acting as wall swirlers, create a swirling flow in the channel (global longitudinal vortex *1*) with a swirl angle at the periphery of the flow core close to the ribs angle. In addition to the global longitudinal vortex, a high-intensity concentrated vortex descends from the trailing edge of the upper face of each edge, in the part of the face that is located upstream *2*. The axis of this edge vortex is first oriented along the

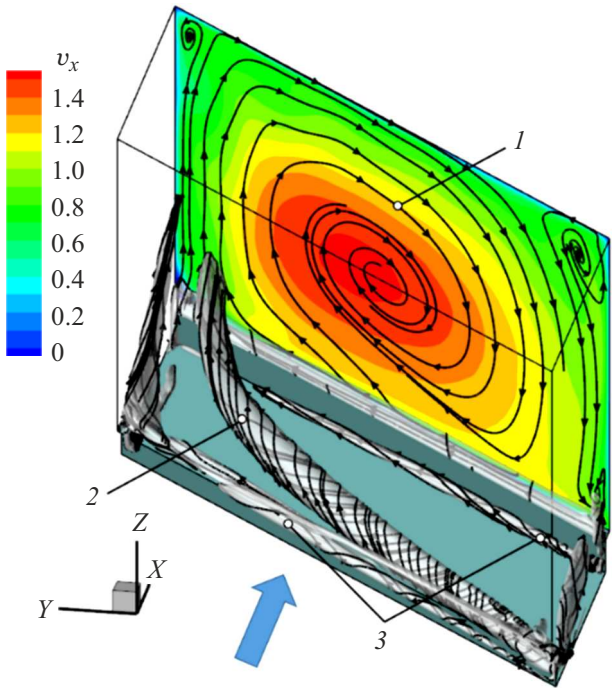

Figure 3. The structure of a developed spatially periodic flow in a channel with a single ribbed wall (according to Ref. [6], $\alpha = 45°$, $\mathrm{Re} = 2 \cdot 10^4$): *1* — distribution of dimensionless longitudinal velocity $v_x = V_x/U_b$ in a channel section parallel to the edge with superimposed projections of swirling streamlines, *2* — isosurface Q-criteria and edge vortex streamlines, *3* — vortices on the upper edge of the rib and in the corner between the rib and the wall.

diagonal of the interrib section, remaining approximately parallel to the plain part of the ribbed wall, and then it abruptly changes its direction and the edge vortex is involved in a global vortex. Less intense vortices *3* are also visible in Fig. 3. They are formed above the upper edge of the rib and in the corner between the edges of the rib and the channel wall.

1. Problem definition and methodological aspects

This paper addresses the problem of numerical simulation of turbulent flow and convective heat transfer of an incompressible medium (air) with a Prandtl number equal to 0.7 in a rectangular channel ($W/H = 1.5$), shown in Fig. 4. The channel consists of an initial plain section *1* with a length of $6H$ ($5.6D_h$), a ribbed section *2* with a length of $60H$ ($50D_h$) and a plain output section *3* length of $16H$ ($13.5D_h$). The ribbed part consists of sixty segments (one segment is shown in Fig. 1). The ribs are installed at an angle of $\alpha = 45°$ with a spacing of $P = H$. The total length of the channel is $69.1D_h$.

Unsteady Reynolds equations (Unsteady RANS) are solved using the SST $k-\omega$ turbulence model [10]. The turbulent Prandtl number is assumed to be 0.9.

The no-slip condition and constant temperature are set on the solid surfaces of the channel. The distributions of velocity, temperature and turbulence characteristics are defined in the inlet section of the initial plain section *1*, which were previously calculated when solving the problem of stabilized flow and developed heat exchange in a plain channel. The methodology and results of these auxiliary calculations are described in Ref. [6]. A zero overpressure value is prescribed in the outlet section of the plain outlet section *3*.

The calculations were performed using the ANSYS CFX 2019 R3 software package. Convective flows were sampled according to the scheme of an increased approximation order (*High Resolution*). The calculated grids consisted of hexahedra, with a total of 10^6 nodes per a rib pitch (segment). The total dimension of the grid, including the sections before and after the ribbing, was $65.4 \cdot 10^6$ nodes. The experience of numerical solution of the problem of spatially periodic flow and heat transfer presented in Ref. [6], based on a special study of grid convergence, allowed determining the requirements for the dimension of the grid. It was shown, in particular, that the difference in the results of the solution on a grid of 10^6 nodes compared with a grid-converged solution on a grid of $68 \cdot 10^6$ was 0.9% in terms of the resistance coefficient and 2.6% in terms of the Nusselt number when calculating the periodic flow in one section of the ribbed channel, performed for $\mathrm{Re} = 2 \cdot 10^5$.

The second-order accuracy scheme was used for advancing in the physical time. The highest frequency fluctuations of the flow were resolved at about 20 time steps. Preliminary calculations showed that about 350 time steps were required to enter a statistically stable mode, starting from the initial approximation, which was an iteration-

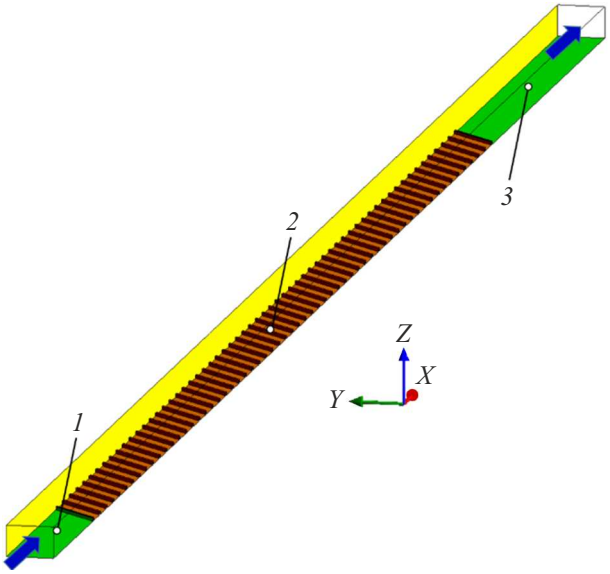

Figure 4. Calculation area: *1* — initial section, *2* — ribbed section, *3* — output section.

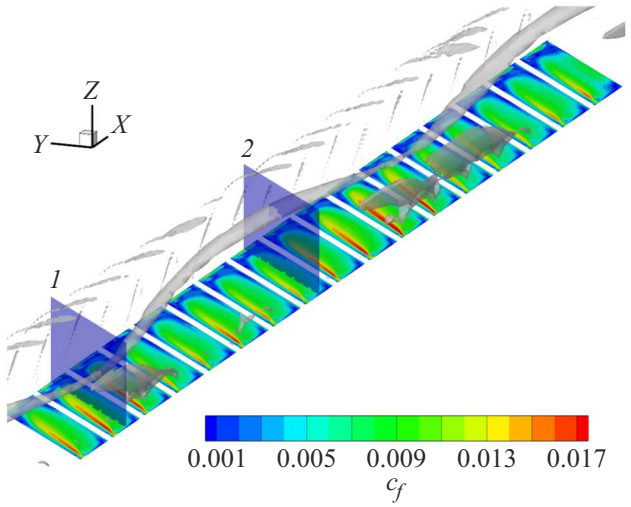

Figure 5. Distributions of local values of the friction coefficient on surfaces in the spaces between the ribs and the positions of isosurfaces on which $R_v = 1.12$; cross section *1* is located in segment 21, section *2* is in the segment 27 (calculation results for $\mathrm{Re} = 2 \cdot 10^5$).

inconsistent solution provided by a stationary problem solver. Given this result the option of averaging the flow parameters carried out over the next 150 steps was included after completing the first 500 steps.

2. Results and discussion

The results of calculation of the time-averaged flow and heat transfer in the channel illustrated in Fig. 4, the ribbed part of which, as noted above, consists of sixty segments, are presented and analyzed below. The numbering of segments and ribs starts from the inlet. The data obtained for four values of the number Re are discussed: 10^4, $5 \cdot 10^4$, 10^5 and $2 \cdot 10^5$.

Fig. 5 shows the flow characteristics in the channel section from segment 20 to segment 36 for the variant with the Re number $= 2 \cdot 10^5$. The figure shows a ribbed wall, the plain sections of which are colored in accordance with the local values of the friction coefficient $c_f = 2\tau_w/\rho U_b^2$. Highlighted and translucent volumetric areas of gray color are formed by isosurfaces of the normalized vorticity value $R_v = |\mathrm{rotV}|H/U_b = 1.12$; $R_v < 1.12$ inside the volumes. Periodically recurring „discontinuous“ volumes pertain to the edge vortices descending from the ribs. The „tube“ extending along the channel defines a formed helical region with relatively low vorticity in the core of the flow ($R_v \le 1.12$). The figure also shows two inclined sections of the channel parallel to the ribs and located in the middle of plain sections of segments 21 (section *1*) and 27 (section *2*). These sections are constructed for a visual identification of the position of the tube $R_v = \mathrm{const}$ relative to the channel walls. The figure clearly shows that the transverse position of the slightly swirling core varies along the channel with a spatial period significantly greater than the rib pitch. A comparison of the flow fields obtained by averaging over individual fragments of the total sample also allowed concluding that the formed helical region is quasi-stationary.

Next, let's pay attention to the distribution patterns of the coefficient c_f. Red-yellow bands with values c_f from 0.013 to 0.017 are distinguished on the interrib plain surfaces of each segment. These bands of increased values c_f occur as a result of the action of edge vortices of the same type as the vortex shown in Fig. 3 on the wall flow. It is very noteworthy that the size and intensity of the color of the bands with increased values c_f change from segment to segment. The larger bands are more brightly colored in red and yellow, while the smaller stripes are less intensely colored and contain almost no red color.

Let us compare the color change of plain surfaces by values c_f with the behavior of a helical isosurface $R_v = 1.12$. The trace of the selected tube is close to the ribbed surface in section *1*, and the trace is located at a distance from the ribbed surface in the cross section *2*. Accordingly, the band imprinting the action of the edge vortex has a larger and brighter size on the interrib wall of segment 21, and the corresponding band is much less pronounced on the interrib wall of segment 27. The same pattern can be traced further along the channel, namely, the approach of the surface $R_v = 1.12$ to the ribbed wall increases friction under edge vortices, removal of the area reduces the friction.

Fig. 6 shows flow patterns in several cross sections normal to the channel axis, located approximately in the same places as the inclined sections in the previous figure; the x coordinate here is counted from the beginning of the ribbed section. In schematic Fig. 1, for example, blue dotted lines show the same type of cross section and the numbering sequence of ribs n and $n+1$ intersecting the current section. The flow patterns in Fig. 6 are shown under the assumption that the observer is looking downstream. The sections of the ribs 22 and 23 are visible in the upper row in the flow patterns, and the sections of the ribs 27 and 28 are visible in the bottom row. The cross sections in the figure include segment 22 with parts of segments 21 and 23 (top row), as well as segment 27 with parts of segments 26 and 28 (bottom row). The sections of the ribs 23 and 28 are located closer to their beginning relative to the direction of flow, and the sections 22 and 27 are located closer to the end.

The left column of the patterns in Fig. 6 shows the distributions of the dimensionless longitudinal velocity $v_x = V_x/U_b$, and the right column shows the distributions of the dimensionless transverse velocity modulus $v_{yz} = (V_y^2 + V_z^2)^{0.5}/U_b$. White lines in the distribution patterns v_x are contours of the surface section $R_v = 1.12$. The arrows indicate the direction in which the contours are moving. It is clearly seen that the surface $R_v = 1.12$ is close to the ribbed wall in the region of segment 22, and the situation is reversed in the region of segment 27. The

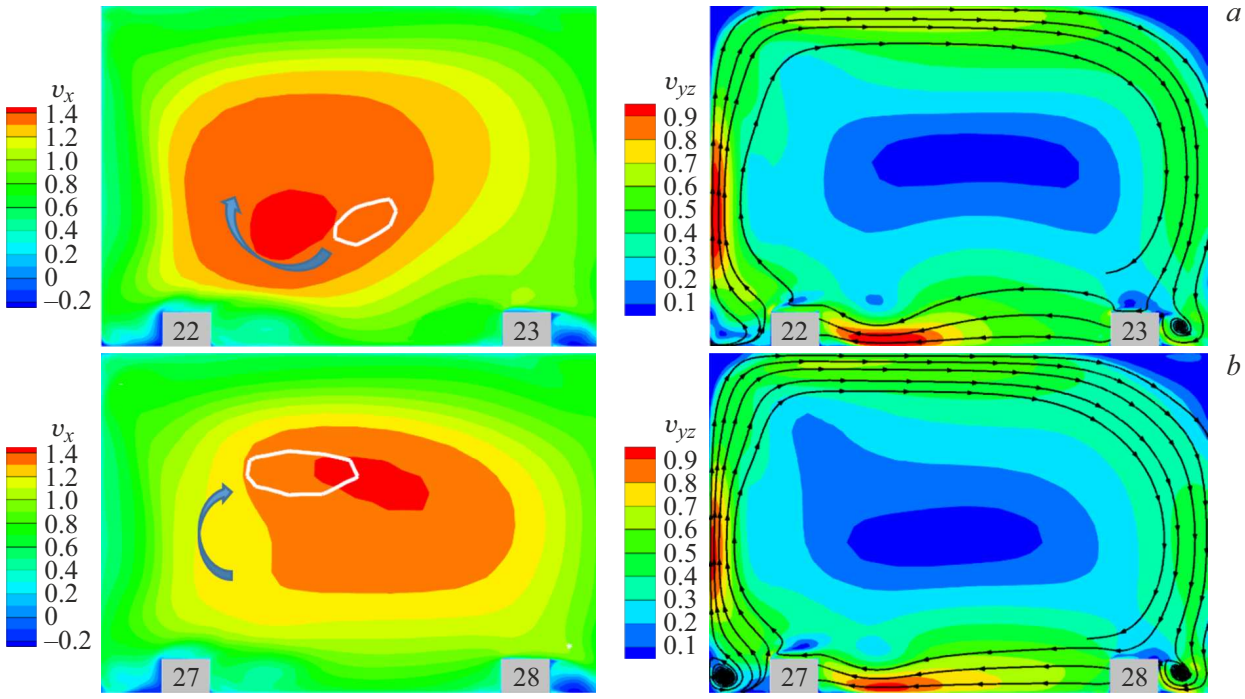

Figure 6. Velocity fields in two sections of the ribbed part, calculated with $\mathrm{Re} = 2 \cdot 10^5$: *a* — section $x/P = 22.25$, *b* — section $x/P = 27.25$; left — longitudinal velocity distributions v_x, on the right — transverse velocity modulus distributions v_{yz} and transverse streamlines; white lines on maps v_x — tube boundaries $R_v = 1.12$; curved arrows — the direction of movement of the tube section boundary between segments 22 and 27; 22, 23, 27 and 28 — rib numbers.

contour $R_v = 1.12$ and the maximum longitudinal velocity area $v_x \geq 1.4$ move synchronously between the sections $x/P = 22.25$ and $x/P = 27.25$. All this provides additional evidence that the flow is characterized by a long-period helical structure at least in the core of the flow.

The transverse flow patterns are shown in Fig. 6 as the distributions of the transverse velocity modulus v_{yz} and the streamlines constructed from the velocity components v_y and v_z. The direction of the secondary flow is consistent with the angle of inclination of the ribs. The defining role of the ribs in creating the swirl of the main flow is also confirmed by the fact that v_{yz} has the highest values at the periphery of the cross sections. In general, the level of transverse velocity at the periphery is about half of the average flow rate velocity V_b. Local elongated regions are observed near the ribbed wall and the lateral left wall, where the transverse velocity modulus almost reaches the value V_b. These regions are formed by edge vortices (Fig. 3) at the ribbed wall descending from the edges 23 and 28. These regions at the side wall are created by vortices that descended from the edges 22 and 27. The edge vortex under the combined action of the channel boundaries and the general swirl of the flow spreads upward and along the side wall as graphically illustrated in Fig. 3. Its presence near the side wall is indicated by areas where the values of the transverse velocity modulus almost reach the values of the average flow rate velocity. It should be noted also that the streamlines plotted in Fig. 6 define relatively small vortex regions in the vicinity of the ribbed wall to the right of the rib sections 23 and 28 that can be associated with the origin of edge vortices when the incoming flow is disrupted from the trailing edge of the upper edge of the rib.

The long-period (in comparison with the pitch of the ribs) helical structure of the slightly swirling core of the flow in the channel is clearly shown in Fig. 7, where the „pigtail“ is clearly visible, formed by a fairly regular, multi-turn interlacing of two elongated flow regions characteristic of the central part of the simulated flow. The longitudinal velocity is $v_x \geq 1.4$ inside the red area, i.e. close to the maximum. The transverse velocity modulus is $v_{yz} \leq 0.08$ inside the blue area.

The diagrams of the segment distribution of the average values of the friction coefficient $\langle c_f \rangle$ on plain interrib surfaces are shown in Fig. 8. Horizontal dashed lines on the diagrams indicate the values $\overline{c_f}$, each of which marks the arithmetic mean value of the coefficient $\langle c_f \rangle$ in the section from 20 to 60 of the segment. The values $\overline{c_f}$ for different values of the number Re are listed in the table. Helical isosurfaces of magnitude R_v are shown under each diagram. The values of the constant selected for surface visualization range from 1.1 to 1.3. Isosurfaces R_v are colored according to the distance from a point on the surface to the ribbed wall. The choice of the field of parameter R_v for comparison with the diagram $\overline{c_f}$ is determined by the strong influence

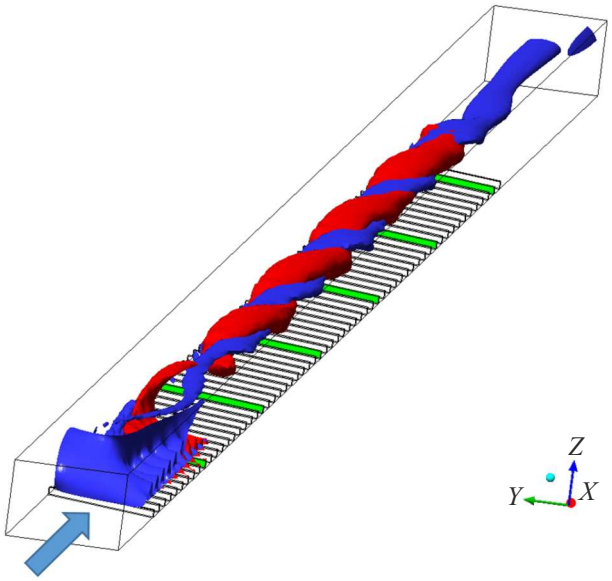

Figure 7. Isosurfaces of a constant value of the longitudinal velocity (red) and a constant value of the transverse velocity modulus (blue), plotted according to the results of calculations for $\mathrm{Re} = 2 \cdot 10^5$. Every tenth rib is colored green.

of the vortex flow structure on the wall convective diffusion transport.

It is possible to record the sequence of phases of flow development in the channel considering together the diagram $\overline{c_f}$ and the shape of the isosurface R_v for each value of the Re number. Let us consider, for example, Fig. 8, *d* pertaining to the variant $\mathrm{Re} = 2 \cdot 10^5$. The friction decreases in the first two segments of the ribbed section (phase *1*). Then, the friction monotonously increases after the segment 2, reaching a maximum in segments 10 and 11 (phase *2*). The increase of friction of these segments is about 75% compared to the segment 2. It can be seen in the image of the isosurface R_v that a longitudinal helical motion begins to form near the ribbed wall in the phase *2*. It is also seen that the formation of a global vortex motion occurs under the influence of both the inclination of the ribs and edge vortices. The edge vortices in this area and downstream can be identified by tracing upward pointed spots of red color. The section from a segment 2 to segment 10 is characterized by the presence of a layer with high vorticity values near the ribbed wall (solid red veil) which explains the monotonous increase of the friction.

The friction decreases to a value close to the value in segment 2 after segment 11 and up to segment 15 (phase *3*). Fig. 8, *d* shows that the friction decreases when breaks appear in the red veil, which reflects the fact of a decrease of wall vorticity. The traces of edge vortices become dotted, and friction reaches a local minimum in the vicinity of segment 15. The degeneration of the traces of edge vortices indicates their weakening or, rather, their movement away from the wall. The formation of the dextral helical shape of the isosurface R_v is almost completed in the vicinity of segment 15.

The forming helical structure is located at a distance from the ribbed wall over five segments (from segment 13 to segment 18), and friction does not change much in the section from segment 15 to segment 22, having an average level, the same as in the rest of the downstream part of the channel (phase *4*). The behavior of friction in this section, if we do not consider the remaining part of the channel, beyond the segment 22, gives reason to conclude that there is some stabilization of the flow when approaching the segment 15. It should be noted that this conclusion is consistent with the data on the length of the initial section in unilaterally ribbed channels given by other authors [3]. If we do not consider the remaining part of the channel, we could assume that the friction should monotonously decrease after segment 17. However, Fig. 8, *d* shows that the isosurface R_v approached the wall in the area covering segments 18–22, the edge vortices also approached it, while friction started to increase instead of decreasing. Phase *4* is intermediate and therefore it partially includes segments that can be attributed to the previous phase *3*, and partially to the next phase *5*.

The helical shape of the isosurface R_v with four screw pitches is defined from segment 19 to the end of the channel (phase *5*). The screw pitches h are almost the same over this phase and have a size of about ten interrib pitches ($h \cong 10P$). The edge vortices approaching the wall become noticeable at each pitch of the screw, as it approaches the wall. The screw tube approaching the wall increase the friction like the edge vortices with it. The friction in the corresponding segments decreases when the screw tube and the edge vortices move away from the wall.

Comparing the parts of Fig. 8, it is possible to note trends in the change of phase boundaries and some other characteristics depending on the Reynolds number. The length of phase *2* decreases from 12 to 8 segments with an increase of the Re number from 10^4 to $2 \cdot 10^5$, the length of the phase *3* also decreases. It is 9 segments for $\mathrm{Re} = 10^4$, and it decreases from 6 to 5 segments for the remaining values of Re. The maximum value of $\overline{c_f}$ significantly exceeds the value of $\langle c_f \rangle$ for all Re numbers at the end of the phase *2*. This excess grows with an increase of the Re number and amounts to 43% at $\mathrm{Re} = 10^4$, 60% at $\mathrm{Re} = 5 \cdot 10^4$, 64% at $\mathrm{Re} = 10^5$ and 67% at $\mathrm{Re} = 2 \cdot 10^5$.

The pitches h of the helical shape of the surfaces $R_v = \mathrm{const}$ decrease in phase *5* with the increase of the Re number. For instance, the pitches h are $12P$ and $11P$ for $\mathrm{Re} = 10^4$ and $5 \cdot 10^4$, respectively, and the pitches h are $10P$ and $9P$ for $\mathrm{Re} = 10^5$ and $2 \cdot 10^5$. At the same time, with the range of fluctuations of the coefficient $\langle c_f \rangle$ decreases relative to $\overline{c_f}$ an increase of the Re number: it amounts to 49% at $\mathrm{Re} = 10^4$, 36% at $\mathrm{Re} = 5 \cdot 10^4$, 32% at $\mathrm{Re} = 10^5$ and 30% at $\mathrm{Re} = 2 \cdot 10^5$. The table shows the values of the average friction coefficients $\overline{c_f}$ on the interrib surface and the values of the same coefficients $\langle c_f^{SP} \rangle$ for the developed spatially periodic (*SP* — Spatial Periodic) flow (according

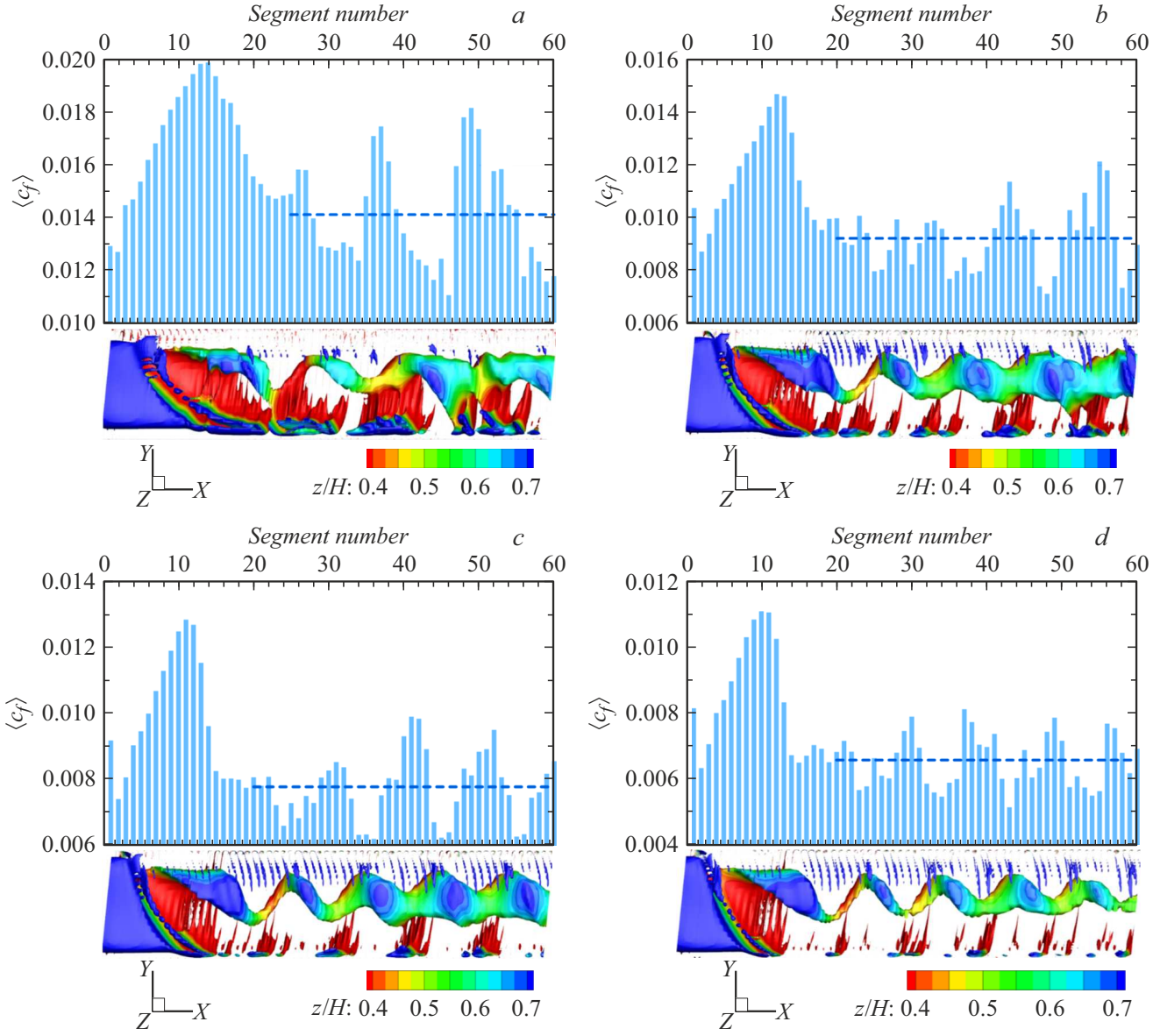

Figure 8. Distribution diagrams $\langle c_f \rangle$ and change of the shape of isosurface R_v along the channel: $\mathrm{Re} = 10^4$ (*a*), $5 \cdot 10^4$ (*b*), 10^5 (*c*), $2 \cdot 10^5$ (*d*); dashed lines — values $\overline{c_f}$.

to data from Ref. [6]). As can be seen, the relative difference between these values $|\overline{c_f} - \langle c_f^{SP} \rangle| / \langle c_f^{SP} \rangle \cdot 100\%$ turned out to be small. It is maximum at $\mathrm{Re} = 10^4$ and is 8.5%, and in other cases it is noticeably less: 4% at $\mathrm{Re} = 5 \cdot 10^4$, 1.3% when $\mathrm{Re} = 10^5$ and 5.7% at $\mathrm{Re} = 2 \cdot 10^5$.

Fig. 9 shows diagrams constructed for the heat transfer intensification parameter $\langle \varepsilon_q \rangle$. The parameter $\langle \varepsilon_q \rangle$ is defined as the ratio $\langle \alpha_{rw} \rangle / \alpha_{sm}$, in which $\alpha_{rw} = q_{rw} / |T_w - T_b|$ and $\langle \alpha_{rw} \rangle$ — local and average heat transfer coefficients on the plain part of the ribbed wall for one segment, q_{rw} and T_b — local heat flow and mass-weighted average temperature in the cross section of the channel parallel to the ribs and located in the middle between them, α_{sm} — heat transfer coefficient in a plain channel with the same hydraulic diameter value. Coefficient $\alpha_{sm} (\alpha_{sm} = Nu_{sm} \lambda_g / D_h$, λ_g — thermal conductivity of the medium, D_h — hydraulic diameter of the channel) is calculated (using the Nikuradze formula for the resistance coefficient [11] $\lambda_{sm} = 0.0032 + 0.221/\mathrm{Re}^{0.237}$) according to Gnielinski's formula for $\mathrm{Re} = 10^4$ [12]:

$$Nu_{sm} = \frac{(\lambda_{sm}/8)(\mathrm{Re} - 1000)\mathrm{Pr}}{1 + 12.7(\lambda_{sm}/8)^{1/2}(\mathrm{Pr}^{2/3} - 1)}$$

and Petukhov-Kirillov formula for $\mathrm{Re} \geq 5 \cdot 10^4$ [13]:

$$Nu_{sm} = \frac{(\lambda_{sm}/8)\mathrm{RePr}}{1 + 900/\mathrm{Re} + 12.7(\lambda_{sm}/8)^{1/2}(\mathrm{Pr}^{2/3} - 1)}.$$

The values of α_{sm} are listed in the table.

It is possible to conclude comparing the diagrams in Figs. 8 and 9 that their shape is similar, which is

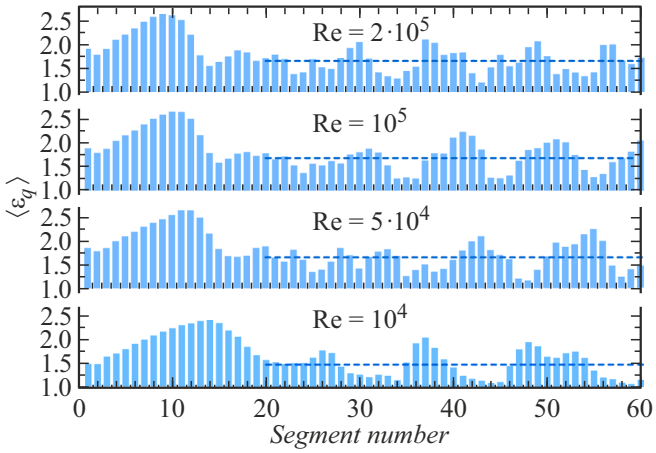

Figure 9. Distribution of the heat transfer intensification parameter $\langle \varepsilon_q \rangle$ along the channel, dashed lines $\overline{\varepsilon_q}$ denote values for spatially periodic flow (according to [6]).

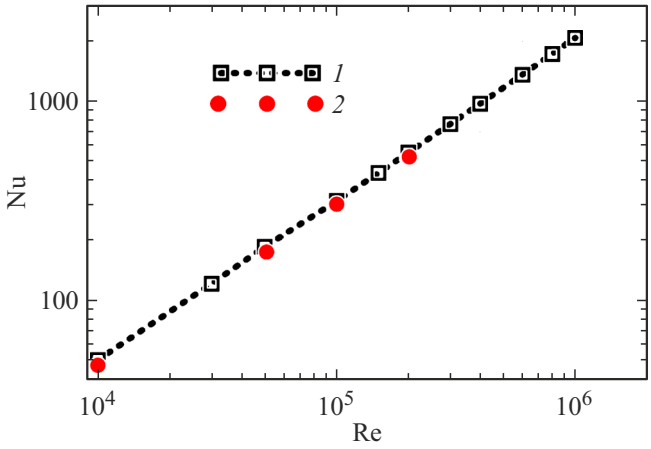

Figure 10. Calculated average values of the number Nu depending on the Re number: *1* — assuming the spatial periodicity of the flow [6,14], *2* — in the section of the helical flow in a long channel.

an expected consequence of the similarity of turbulent convective-diffusive heat and momentum transfer. It was shown in Ref. [6] that the Reynolds analogy coefficient $2\mathrm{St}/c_f$ ($\mathrm{St} = \mathrm{Nu}/(\mathrm{RePr})$ — the Stanton number, in which the Nusselt number is determined by the heat transfer on all walls) remains close to one, varying from 0.9 to 1.1 in the range of values of the Re number considered here.

The comparison of the diagrams in Fig. 9 with the graphs in Fig. 2 can show that the behavior of the experimental heat transfer intensification curves in the first fifteen to twenty segments is similar in many respects to the calculated diagrams. Phases *1–4* of the development of flow identified during the analysis of the calculated data can also be identified on experimental graphs. The phase *5*, pertaining to the formed helical motion in the core of the flow, is not visible on the graphs, with the exception of variant 2, which can be explained by the insufficient number of segments (less than 16) in the experimental channels of the variants *1, 3* and *4*.

The horizontal dashed lines on the diagrams $\langle \varepsilon_q \rangle$ mark the values $\overline{\varepsilon_q}$, each of which represents the arithmetic mean of the values $\langle \varepsilon_q \rangle$ in the segment from 20 to 60 segments (in the phase section *5*). The values $\overline{\varepsilon_q}$ calculated for different Re numbers are listed in the table. The table shows the values of the average heat transfer intensification coefficients

Integral characteristics of friction and heat transfer

Re number	10^4	$5 \cdot 10^4$	10^5	$2 \cdot 10^5$
$\overline{c_f}$	0.0141	0.0092	0.0078	0.0066
$\langle c_f^{SP} \rangle$	0.0130	0.0096	0.0079	0.0070
$\overline{\varepsilon_q}$	1.45	1.63	1.69	1.69
$\langle \varepsilon_q^{SP} \rangle$	1.53	1.81	1.88	1.91
$\alpha_{sm}(\mathrm{W/m^2 \cdot K})$	7.0	23.3	38.9	67.5

on the interrib surface $\langle \varepsilon_q^{SP} \rangle$ for the developed spatially periodic flow in addition to the values of $\overline{\varepsilon_q}$ [6]. The relative difference between these values $\overline{\varepsilon_q} - \langle \varepsilon_q^{SP} \rangle / \langle \varepsilon_q^{SP} \rangle \cdot 100\%$ was: 5.2% at $\mathrm{Re} = 10^4$, 10% at $\mathrm{Re} = 5 \cdot 10^4$, 10.1% at $\mathrm{Re} = 10^5$ and 11.5% at $\mathrm{Re} = 2 \cdot 10^5$. Thus, the difference between the average values $\overline{\varepsilon_q}$ from the values obtained for the idealized spatially periodic flow $\langle \varepsilon_q^{SP} \rangle$ remains within the range close to ten percent with the formed helical motion (phase *5*), as in the case of average values of friction coefficients.

Fig. 10 shows the dependences of the average Nusselt number calculated taking into account the heat transfer on all walls of the channel on the Reynolds number. The heat transfer is approximated by the dependence $\mathrm{Nu}^{SP} = 0.0295 \cdot \mathrm{Re}^{0.807}$ for the periodic flow, a close correlation $\mathrm{Nu} = 0.0288 \cdot \mathrm{Re}^{0.804}$ is valid for a long channel in the section of the helical flow.

Conclusions

1. The core of a statistically stationary turbulent flow has a helical shape in the chosen configuration of a long (gauge 50) ribbed channel, the characteristics of which depend on the Reynolds number in the conditions that we studied.

2. The process of formation of a helical structure along the length of the channel for all values of the Reynolds number can be divided into four phases, followed by entering the (fifth) phase of a fully developed helical motion of the medium with a screw pitch and an amplitude of change of the hydrodynamic characteristics monotonously dependent on the Reynolds number.

3. The sections where the helical structure of the flow core is gradually formed, as a whole, occupy about a third of the length of the channel, their length slightly decreases with an increase of the Reynolds number. The process

of a helical structure formation is accompanied by non-monotonic behavior of friction and heat transfer, while the friction and heat transfer reach extremely high values in the initial phases.

4. The resistance and heat transfer characteristics averaged over the channel length within 10% coincide with the characteristics calculated earlier in Ref. [6] for an idealized spatially periodic flow in the phase with a fully developed helical structure.

5. The phases of formation of the helical structure of the flow core in ribbed channels identified as a result of calculations are indirectly (through heat transfer characteristics) found in the results of a number of experimental studies in Ref. [5,7,8].

Acknowledgment

The study results were obtained using the computational resources of the supercomputing center of Peter the Great St. Petersburg Polytechnic University (www.spbstu.ru).

Funding

The study was funded by a grant of the Russian Science Foundation № 23-29-00094.

Conflict of interest

The authors declare that they have no conflict of interest.

References

[1] E.K. Kalinin, G.A. Dreitser, I.Z. Kopp, A.S. Myakotchin. *Efficient surfaces for heat exchangers: fundamental and design* (Begell, 2002), 392 p. DOI: 10.1615/978-1-56700-167-9.0
[2] V.I. Terekhov, A.Yu. Dyachenko, Y.J. Smulsky, T.V. Bogatko, N.I. Yarygina. *Heat transfer in subsonic separated flows* (Springer, 2022), 230 p.
[3] J.-C. Han, S. Dutta, S. Ekkad. Gas Turbine Heat Transfer and Cooling Technology (CRC Press, 2013), 865 p.
[4] M.K. Dwivedi, M. Choudhary. Mater. Today: Proceedings, *63*, 272 (2022). https://doi.org/10.1016/j.matpr.2022.03.072
[5] I. Baybuzenko. *Proceedings of the ASME. Turbo Expo 2021.* (2021) 5B. https://doi.org/10.1115/GT2021-00259
[6] V.V. Ris, S.A. Galaev, A.M. Levchenya, I.B. Pisarevsky. Teploenergetika **2**, 80 (2024) (in Russian). DOI: 10.56304/S0040363624020085
[7] A.P. Rallabandi, H. Yang, J. Han. J. Heat Transfer, **131**, 071703 (2009). https://doi.org/10.1115/1.3090818
[8] G. Tanda, R. Abram. J. Turbomachinery, **131**, 021012−1 (2009). DOI: 10.1115/1.2987241
[9] M. Molki, E.M. Sparrow. J. Heat Transfer, **108**, 482 (1986).
[10] F. Menter, M. Kuntz, R. Langtry. *Turbulence, Heat and Mass Transfer 4* (Begell House Inc., 2003), p. 625−632.
[11] L.G. Loytsiansky, *Mekhanika zhidkosti i gaza* (Drofa, M., 2003), 840 s. (in Russian).
[12] T.L. Bergman, A.S. Lavine, F.P. Incropera, D.P. DeWitt. *Fundamentals of Heat and Mass Transfer* (John Wiley & Sons., 2011), 1076 p.
[13] B.S. Petukhov, V.V. Kirillov. Teploenergetika **4**, 63 (1958) (in Russian).
[14] A.M. Levchenya, S.A. Galaev, V.V. Ris. Nauchno-tekhnicheskie vedomosti St. Petersburg State Polytechnical University Journal. Physics and Mathematics, **17** (4), (2024) DOI: https://doi.org/10.18721/JPM.17403 (in Russian).

Translated by A.Akhtyamov